Correlation of precipitation kinetics with Vickers hardness in Haynes® 282® superalloy: *In-situ* high-energy SAXS/WAXS study

Sylvio Haas[1,a], Joel Andersson[2,b], Martin Fisk[3,c,d], Jun-Sang Park[4,e], Ulrich Lienert[5,a]

[a]Photon Science, DESY, Hamburg, Germany

[b]Department of Engineering Science, University West, Trollhättan, Sweden

[c]Materials Science and Applied Mathematics, Malmö University, Malmö, Sweden

[d]Division of Solid Mechanics, Lund University, P.O. Box 118, SE-221 00 Lund, Sweden

[e]X-ray Science Division, Advanced Photon Source, Argonne National Laboratory, USA

[1]Sylvio.Haas@desy.de, [2]Joel.Andersson@hv.se, [3]Martin.fisk@mah.se, [4]parkjs@aps.anl.gov,
[5]Ulrich.Lienert@desy.de

Abstract

The aim of this work is to characterize the precipitation kinetics in Haynes® 282® superalloys using *in-situ* high-energy Small Angle X-ray Scattering (SAXS) together with Wide Angle X-ray Scattering (WAXS). The phases identified by WAXS include γ (matrix), γ' (hardening precipitates), MC (metallic carbides), and $M_{23}C_6$ /M_6C (secondary metallic carbides). The γ'-precipitates are spheroids with a diameter of several nanometres, depending on the temperature and ageing time. From the SAXS data, quantitative parameters such as volume fraction, number density and inter-particle distance were determined and correlated with *ex-situ* Vickers microhardness measurements. The strengthening components associated with precipitates and solid solutions are differentiated using the measured Vickers microhardness and SAXS model parameters. A square root dependence between strengthening attributable to the precipitates and the product of volume fraction and mean precipitate radius is found. The solid solution strengthening component correlates with the total volume fraction of precipitates.

1 Introduction

Superalloy possesses unique properties regarding strength and thermal stability at elevated temperatures. The excellent high-temperature properties are primarily associated with specific hardening phases that are present in these types of alloys. Such alloys typically find use in aero engines and land based turbines [1]. The most widely used superalloy in aero and land based turbines is Alloy 718, which comprises more than 50% of the superalloy usage today. It benefits from the γ'' hardening phase, which has a stoichiometry Ni_3Nb. However, the strength reduces above approximately 650°C, which is the service temperature limit of this alloy.

Alloys capable of withstanding higher temperature are needed to improve turbine efficiency. Alloys such as the newly developed Ni-based superalloy Haynes® 282® are now available. This alloy can withstand higher temperatures (approximately 800°C) without significant loss in load-carrying ability [2–6]. Haynes® 282® contains smaller amounts of iron and niobium, but larger amounts of aluminium, titanium and molybdenum, making it a γ' hardening alloy while Alloy 718 is a γ'' hardening alloy. The nominal compositions of Alloy 718 and Haynes® 282® are given in the supplementary information.

Haynes® 282® was developed by Haynes International in 2005. The stoichiometry of the γ'-phase is nominally $Ni_3(Al,Ti)$, which nucleates in the matrix as spheroids [3]. Since the unique high temperature properties are governed by the nanometre sized γ'-phase, it is of great importance to understand the kinetics of precipitation. This is not only of importance when designing or optimizing the heat treatment of this and similar alloys, but is also of interest when processing the alloy or using it in various types of manufacturing processes [2,7–10]. The γ' hardening alloys are known to harden rapidly, which in turn creates difficulties during primary (e.g. rolling and forging) and secondary (e.g. welding and machining) processing.

The γ'-precipitates are approximately 20-50 nm in radius after full ageing. This makes quantification using optical microscopy impossible and difficult even using scanning electron microscopy (SEM). Furthermore, it is also impossible to quantify the early stages of precipitation using tools such as transmission electron microscopy (TEM) or atom probe analysis. In addition, such tools only provide information from a very small amount of material, and no significant understanding of the volumetric content of precipitates is obtained. To date, there have been no investigations of the early stages of precipitation of the γ'-phase in Haynes® 282®, to the authors' knowledge.

The aim of this study is to investigate the precipitation kinetics of the hardening γ'-phase present in Haynes® 282® using *in-situ* high-energy Small Angle X-ray Scattering (SAXS) combined with Wide Angle X-ray Scattering (WAXS). These experiments provide volumetric information concerning precipitation in terms of: number; size distribution; and inter-particle spacing during nucleation and growth [11,12]. The advantage of using high-energy X-rays (e.g. 87 keV), compared with those more commonly produced from medium-range X-ray sources (5-15 keV), is the significant increase in penetration depth. This enables the investigation of superalloys in their bulk form. In this study samples 2 mm in thickness were used (*c.f.* samples 50 µm in thickness used in transmission geometries for medium-range X-ray energies [11]). *In-situ* thermo-mechanical testing was performed on these thick samples to simulate a more realistic, real-world condition. In the second part of this study, precipitation kinetics is correlated with *ex-situ* Vickers microhardness measurements. It is found from the experimental data that the hardness correlates with the square root of the product of volume fraction and mean radius of the γ'-precipitates.

2 Experimental methods

The following section describes the experimental methods used for microhardness tests and combined *in-situ* high-energy SAXS and WAXS measurements.

2.1 *Ex-situ* microhardness measurements

Test specimens made from 2 mm thick Haynes® 282® sheets, of chemical composition given in the supplementary information, were prepared by solution heat treatment at 1120°C for 30 minutes.

These were used for heat treatment experiments and Vickers microhardness testing using a load of 200 g for 15 s. Heat treatment experiments were carried out at 12 levels within the temperature range 600-1000°C (600, 650, 700, 750, 775, 800, 825, 850, 875, 900, 950 and 1000°C) for seven dwell times within the range 1-240 min (1, 5, 10, 30, 60, 120 and 240 min). The heat treatments were performed in a small lab furnace that enabled rapid heating after the specimen was inserted into the oven. The ageing time commenced when the temperature reached the ageing temperature. The temperature was measured using a type-K thermocouple attached to the specimen. To avoid the effect of grain boundaries on the results of Vickers testing, each specimen was lightly etched electrolytically at 4 V using oxalic acids. Three hardness indentations were made on each specimen for the given ageing time and temperature.

2.2 *In-situ* SAXS and WAXS measurements

A combined high-energy SAXS and WAXS experiment was performed at the Advanced Photon Source (APS), Argonne National Laboratory, USA. Haynes® 282® sheet material of thickness 2 mm, delivered in mill annealed condition (1120°C for 30 min and slowly cooled to room temperature), was used in this study, Figure 1. The specimens from the sheet were prepared using water jet machining, which is assumed not to induce any significant heating during cutting. The samples were first solution heat treated at 1010^{o}C for 2 hours in a vacuum furnace followed by convection cooling using argon to minimize the volume fraction of the hardening phase and to stabilize the carbides in the initial state.

Two Haynes® 282® samples were aged *in-situ* for 1 hour at 760°C and 820°C. The experiments were carried out at beamline 1-ID-E at the APS [13] using an X-ray energy of 87 keV. The beam was vertically focused using refractive lenses, such that the focus was at the SAXS detector. The beam was horizontally defined using slits. The beam size at the sample position was approximately 300 x 150 µm² (h x v). Each specimen was surrounded by an infrared radiation furnace capable of heating to 1200°C at a heating rate of 120°Cs^{-1}. A rapid heating rate is important as it reduces pre-precipitation. The sample temperature was measured with a type-K thermocouple spot-welded onto the sample. The WAXS pattern was recorded with the Hydra setup consisting of four GE flat panel detectors [14] at a sample to detector distance of 2.63 m with an exposure time of 0.3 s. The SAXS pattern was recorded using a PIXIRAD CdTe photon counting detector [15], with a nominal pixel size of 60 µm in a hexagonal arrangement and an exposure time of 2 s. The distance between the sample and the detector was 6.56 m. The primary beam was blocked by a 300 µm wide tungsten beam stop in front of the SAXS detector. The primary flux and the transmitted beam intensity were measured using ionization chambers before and after the sample, respectively.

Cerium oxide and silver behenate were used to determine detector parameters for WAXS and SAXS respectively. With these detector parameters, the magnitude of the scattering vector, q, covered by the respective area detectors could be determined. A pre-calibrated glassy-carbon sample of thickness 3 mm was used to scale the SAXS intensities to differential scattering cross section (cm^{-1}).

3 Results and discussion

The Vickers microhardness measurements are given in Section 3.1, followed by a WAXS pattern analysis to determine the crystallographic phases and domain sizes. The phases identified by WAXS were the matrix γ-phase, the precipitate γ'-phase, primary metallic carbides MC, and secondary metallic carbides $M_{23}C_6$/M_6C. Precipitate characterization is described in Sections 3.3 and 3.4 for

SAXS and WAXS, respectively. In Section 3.5 the change in microhardness caused by the ageing process is compared and correlated with the findings from the quantitative SAXS analysis.

3.1 Vickers microhardness

Figure 2 shows Vickers microhardness data. Figure 2a) shows the measured hardness as a function of temperature and ageing time. Figure 2b) shows the variation in microhardness with ageing time for five temperatures (750, 775, 800, 825 and 850°C). The figures indicate that peak hardness is achieved when the material is aged at 825°C, with continued increases even after 240 min of ageing. Ageing at 850°C gives a lower peak hardness, which plateaus after 60 min of ageing. Peak hardness is not achieved with ageing temperatures lower than 825°C, even after 240 min of ageing.

3.2 Microstructure characterization using WAXS

In Figure 3, the azimuthally-integrated (over all four GE flat panel detectors) WAXS diffraction from a sample at its initial state at room temperature is shown. It reveals intense peaks, corresponding to the sum of the γ-phase and γ'-phase, and several weak peaks, corresponding to three identified phases: γ', metallic carbide MC (M=Ti, Mo), and secondary metallic carbides $M_{23}C_6$ and/or M_6C. The secondary metallic carbides are formed by the following phase transformation path: $\mathrm{MC} + \gamma = \mathrm{M}_{23}\mathrm{C}_6$ and/or $\mathrm{M}_6\mathrm{C} + \gamma'$ [16]. The lattice parameters of the phases described above were determined by Rietveld refinement [17] using the program MAUD [18]. The lattice parameters are summarized in Table 1. A full quantitative Rietveld refinement was not possible because the measured WAXS diffraction pattern exhibited diffraction spots as a function of azimuth angle, indicating that the initial state of the material consists of large defect free grains. A typical 2D diffraction pattern of the sample is shown in supplementary information. Therefore, the absolute intensities of the peaks fluctuated and could not be refined. The problem of a spotty diffraction pattern rather than a powder like pattern may be overcome by rotating or moving the sample during exposure, such that more grains are exposed to the beam. This was not possible with the sample environment used. Nevertheless, the positions of the peaks from all four GE detectors were statistically identical, confirming the calibrations, and their average value was used to determine the lattice parameter. The azimuthally-integrated *in-situ* WAXS patterns of samples aged at 760 and 820°C are shown in the supplementary information.

The heat treatment was performed in air and the formation of oxides, such as Fe_2O_3, was expected. Although the diffraction patterns do not show any presence of diffraction peaks originating from oxide phases, it is believed that few oxide traces were formed during the ageing process. Furthermore, an additional heat treatment study of the material at higher temperature indicates that oxide formation starts at approximately 1000°C, independent of the heating rate.

3.3 Precipitate characterization using SAXS

The data pre-processing and the SAXS model are discussed in Sections 3.3.1 and 3.3.2, respectively.
In Section 3.3.3 quantitatively extracted parameters are discussed. Correlations between some of the parameters are found and discussed in Section 3.3.4.

3.3.1 Data pre-processing

The isotropic 2D SAXS patterns are azimuthally integrated using the python package pyFAI [19]. The calibration parameters as well as the beam centre were determined from the silver-behenate measurements. The 1D scattering curves obtained in relative units are scaled to absolute differential scattering cross section (cm^{-1}) and background corrected by the following equation [20]

$$I(q,t,T) = \left(\frac{I_s(q,t,T)}{\tau_s(t,T)\cdot I_s^0(t,T)} - \frac{I_e(q,t,T)}{\tau_e(t,T)\cdot I_e^0(t,T)}\right)\cdot f_{abs}, \quad (1)$$

where $I_s(q,t,T)$ and $I_e(q,t,T)$ are the measured intensity of the sample (s) and the measured intensity without sample (empty; e), respectively at a given scattering vector q, time t and ageing temperature T. The empty measurement (without sample) was performed using the same conditions as with the sample. The measured intensity is normalized using the incoming photon flux $I_s^0(t,T)$ or $I_e^0(t,T)$ and by the measured X-ray transmission $\tau_s(t,T)$ or $\tau_e(t,T)$. The transmission of the empty measurement is set to unity for all times and temperatures. The X-ray transmission of the 2 mm thick specimen is in the range 37-39 % for the entire study. The main change of transmission occurs during heating of the specimen. This change is mainly caused by thermal expansion and small movements of the specimen. The observed transmission range in this experiment is close to the signal optimized transmission, which is e^{-1} (36.79%) for scattering experiments. Therefore, multiple scattering effects normally observed in neutron scattering experiments of alloys [21] can be neglected. The time evolution of transmission is shown in the supplementary information. The scaling factor f_{abs} in Eq. (1) is determined using experimentally measured SAXS intensities of the pre-calibrated glassy-carbon sample [20].

3.3.2 SAXS model description

Previous studies using transmission electron microscopy (TEM) and scanning electron microscopy (SEM) of Haynes® 282® [22–26] show that various phases are present in the alloy. Metallic carbide phases with sizes in the range of a few hundred nanometres to a few micrometres are mainly present at grain boundaries. This implies that carbides will contribute significantly to SAXS intensity at q smaller than 0.02 nm^{-1} which is far outside the accessible q-range of the experimental setup used in this work. Previous TEM results reveal that the γ'-phase precipitates within the γ-phase as nanometre-sized spherical particles that are crystalline and maintain this shape for ageing up to 3000h at 788°C [22]. Based on these TEM and SEM results, a two-phase structure model can be assumed to fit the *in-situ* SAXS data. The absolute intensity is given by [27,28]:

$$I(q) = \Gamma \int_0^\infty D(r,\mu,\sigma)\{V(r)F(q,r)\}^2 S(q,r,\beta,\phi_l)dr + c_0 q^{-c_1} + c_2\,, \quad (2)$$

where $F(q,r)$ is the form factor of spherical particles [28] with radius r and volume $V(r)$ at q. $D(r,\mu,\sigma)$ is the normalized size distribution of the precipitates. In general, a lognormal distribution for the radius of the precipitates can be assumed [29,30]

$$D(r,\mu,\sigma) = \frac{1}{\sqrt{2\pi}\sigma\mu\exp(\frac{\sigma^2}{2})}\cdot\exp\left(\frac{-\ln(r/\mu)^2}{2\sigma^2}\right), \quad (3)$$

where μ is the location parameter and σ is the width parameter of the distribution. Because of the expected high volume fraction of precipitates ϕ, inter-particle interaction must be included in the SAXS model by introducing a structure factor $S(q,r,\beta,\phi_l)$ in Eq. (2). There are several approaches for this: the most well-known approximations are the “decoupling approximation” and the “local monodisperse approximation” [31]. The decoupling approximation assumes that the position of particles is independent of their size, whereas the local monodisperse approximation assumes that the position of the particles is completely correlated with their size. The decoupling approximation gives reasonable results for small polydispersity (nearly monodisperse) systems, and the local monodisperse approximation works better for larger polydispersity of 10% and more [31]. Because of the expected relatively large polydispersity of the γ'-precipitates (>10%), the local monodisperse approximation is used in Eq. (2). Furthermore, to keep the number of free fitting parameters as small as possible the hard sphere potential [31,32] is used as the structure factor, with a spherical repulsion radius $r_{hs} = \beta \cdot r$ and local volume fraction ϕ_l of the γ'-precipitates.

As discussed above, the metallic carbides are well outside the detection limit for the q-range of the performed experiment. Scattering from these precipitates is present but has approximately asymptotic character (i.e. decrease in intensity with increasing q) and the size and shape cannot be determined from a scattering curve with such shape. Nevertheless, the scattering from these precipitates must be included in the model. Therefore, the background term $c_0 q^{-c_1}$ has been included. Naturally, no conclusion for size, shape and volume fraction of these precipitates could be drawn from the fit parameters for this particular part of the scattering. The q-independent background term c_2 takes into account fluorescence scattering as well as air scattering. The slowly varying intensity at large q is mainly attributed to small changes of the air scattering. During the *in-situ* measurement, air scattering was measured once at the beginning and subtracted from all sample measurements. Small changes in air scattering with time will be accounted for by the c_2 background term. The scale factor Γ in Eq. (2) is given by the number density of precipitates N and the square of the scattering contrast $\Delta\rho$:

$$\Gamma = N \cdot \Delta\rho^2. \tag{4}$$

Determination of the quantities N and $\Delta\rho$ directly from the fitting is not possible and the scaling factor Γ is used during the first fitting step (Eq. (2)). In the second fitting step, the following system of nonlinear equations is numerically solved to determine N, $\Delta\rho$ and ϕ:

$$\mathrm{N} = \frac{3(-3\mathrm{Q_{inv}} + 8\pi^3 \langle R^3 \rangle \Gamma)}{32\pi^4 \langle R^3 \rangle^2 \Gamma}, \tag{5a}$$

$$(\Delta\rho)^2 = \frac{32\pi^4 \langle R^3 \rangle^2 \Gamma^2}{-9Q_{inv} + 24\pi^3 \langle R^3 \rangle \Gamma}, \tag{5b}$$

$$\phi = 1 - \frac{3Q_{inv}}{8\pi^3 \langle R^3 \rangle \Gamma}, \tag{5c}$$

where $\langle R^3 \rangle$ is the third moment of the size distribution. It is calculated from the fitting result by using the following expression:

$$\langle R^3 \rangle = \int_0^\infty D(r, \mu, \sigma) \cdot r^3 dr. \tag{6}$$

The so-called invariant Q_{inv} is given by [33]

$$\mathrm{Q_{inv}} = \int_0^\infty I(q) \cdot q^2 dq. \tag{7}$$

To experimentally determine the invariant, the SAXS intensities $I(q)$ must be known over the entire q-range. This is not the case for the measured SAXS curves. In lieu of applying the measured intensity in Eq. (7), Eq. (2) (without the two background terms) is used to compute the invariant. In this way, the extrapolation of intensities especially at low q is more accurate compared with the traditional Guinier approximation [33].

3.3.3 Quantitative parameters

Figures 4a) and 4c) show selected SAXS curves (symbols) for ageing at 760 and 820°C, respectively. With increasing ageing time, the broad peak at q = 0.5 nm^{-1} evolves, and shifts towards smaller q. This broad peak indicates the appearance of nanometre size particles. In addition to the experimental data, the corresponding fitted SAXS model curves (solid lines) are shown in Figs. 4a) and 4c) as well. The SAXS model describes the experimental data over the entire measured q-range and ageing. The resultant lognormal size distributions are shown in Figs. 4b) and 4d). The mean precipitate radius increases with ageing time, which can be seen by the peak shift towards a larger radius in the distribution plots.

Nucleation and growth kinetics of the observed particles is more rapid for ageing at 820°C than ageing at 760°C. The increase in noise for high q values is a result of a low signal to background ratio. This means that the intensity of background scattering, which has been removed from the curves, is much higher compared with the scattering from the nano size precipitates. An evacuated flight path from the sample to detector can improve the signal to background ratio.

Figure 5 shows the most relevant model parameters for further interpretation of samples aged at 760 and 820°C as a function of ageing time. The parameters r_{mean} and Γ are direct fitted parameters, while the repulsion zone width is calculated using $w_{hz} = r_{mean} \cdot (\beta - 1)$. The initial states of the two samples are not identical comprising γ'-nuclei of slightly different size and polydispersity. This could be a result of the pre-heat treatment of the samples (mill annealed) or of the cutting process used to prepare the specimens.

Three regions can be identified during the ageing process: I dissolution + nucleation, II nucleation + growth, and III growth + coarsening. These regions are shown in Figure 5. During the heating process and the accompanying first minute of ageing (region I), the mean radius remains approximately constant, whereas the repulsion zone width increases. The width of the repulsion zone near the existing particles is related to the concentration of solute atoms in the matrix (such as a diffusion zone around each particle). An increase of w_{hz} can be understood as an increase in concentration of solute atoms in the matrix-phase. This increase is probably caused by dissolution of existing precipitates. The decrease in the scaling factor Γ in region I of ageing, which is proportional to the number density of particles, also supports the interpretation of dissolution of precipitates in stage I of ageing.

A continuous increase in precipitate size can be seen after short delays of 5.5 and 2.5 min for the 760 and 820°C samples, respectively. This is interpreted as the starting point for nucleation and growth of new precipitates (region II). At the same time, the repulsion zone width begins to decrease, which means the concentration of solute atoms in the matrix decreases. This is because of nucleation and growth of new precipitates.

After roughly 20 minutes of ageing at 820°C, the repulsion zone width becomes constant, whereas the mean radius continues to increase (region III). This indicates that all the solute atoms in the matrix have been used to form the precipitates and the volume fraction of γ'-phase reaches a maximum value (saturation level of precipitates). Such behaviour (a constant volume fraction and increase in precipitate size) is the well-known Ostwald ripening effect, and occurs with the largest particles. The results show that the sample aged at 760°C has not reached this stage of ageing.

The evolution of the volume fraction ϕ, number density N and scattering contrast $\Delta\rho$ of the precipitates are determined by the second analysis step by numerically solving the system of nonlinear equations (Eqs (5a-c)). In the second analysis step, the parameters extracted during the first analysis step (Eq. (2)) are used. The result is shown in Figure 6. The same ageing process regions as for the parameters presented in Figure 5 (I, II, and III) are identified for these parameters as well. Within the first minutes of ageing the volume fraction and number density of particles decrease significantly, and a reduction in volume fraction by up to 50% can be seen. In region II, an increase in volume fraction to its maximum value of roughly 14% occurs; at the same time the scattering contrast decreases.

The scattering contrast is related to the concentration of solute atoms, and decreases during nucleation and growth of new precipitates. In region III, the volume fraction remains constant, whereas the number density slowly decreases further while the mean radius increases. This is classical Ostwald ripening. The small increase in the scattering contrast during Ostwald ripening could be interpreted as a composition change either of the precipitates or the surrounding matrix phase. Interpretation of the evolution of number density in region II is more complicated than that in region I. The total change in number density during the ageing process can be expressed as

$$\Delta N(t,T) = \Delta N_{dissolution}(t,T) + \Delta N_{nucleation}(t,T) + \Delta N_{Ostwald}(t,T). \tag{8}$$

In region II, the change in number density caused by Ostwald ripening is zero and only the dissolution and nucleation terms in Eq. (8) contribute to the overall change in number density. If $|\Delta N_{nucleation}| > |\Delta N_{dissolution}|$ an increase in number density must be present. This increase is the case for the sample aged at 760°C. On the other hand, if $|\Delta N_{nucleation}| < |\Delta N_{dissolution}|$ a further decrease in number density must be present, but with smaller slope, which is the case for the sample aged at 820°C. $\Delta N_{Ostwald}$ is the dominant term in region III, and a decrease in number density is observed. In the supplementary information, a graph with the total change in number density as function of time is shown.

3.3.4 Correlation of quantitative parameters

In Section 3.3.3, the results indicate a correlation between the volume fraction, the repulsion zone width and the scattering contrast. Figure 7 shows these parameters, omitting the volume fraction. Instead, the change in volume fraction in relation to the saturation level $\Delta\phi(t,T) = \phi_{max}(T) - \phi(t,T)$ is shown. A clear correlation between these parameters can be seen. The correlation with scattering contrast is less evident compared with the volume fraction difference and repulsion zone width for increased ageing time.

The number of solute atoms in the surrounding matrix-phase increases with increasing $\Delta\phi$ (i.e. the volume fraction of precipitates decreases). This leads to an increased diffusion zone (increase in repulsion zone width). Because the electron density of the surrounding matrix-phase increases while the electron density of the remaining precipitates stays nearly unchanged, the scattering contrast $\Delta\rho$ increases as well. Therefore, the difference in electron density $\Delta\rho$ increases with increasing $\Delta\phi$. In region II, the change in matrix composition causes a decrease in repulsion zone width and scattering contrast, which decreases $\Delta\phi$. In region III, it is observed that the change in scattering contrast is no longer correlated with the change in volume fraction and repulsion zone width, since precipitation has saturated. We suggest that the change in $\Delta\rho$ is caused by a change in the composition or macroscopic density of either the precipitates or matrix-phase.

3.4 Precipitate characterization using WAXS

The γ'-precipitate domain size may be determined from diffraction line broadening analysis and compared with the precipitate size determined by SAXS. Here, the {100}, {110}, {210} and {211} reflections from the γ'-phase were used to perform a Williamson-Hall analysis [34] to determine the domain size. Because of the assumption of spherical precipitates (isotropic size), mixed reflections were used for the Williamson-Hall analysis. The diffraction peaks were fitted with a Pseudo-Voigt function, and the integral breadths of the Gaussian and Lorentzian contributions were determined from the full width at half maximum (FWHM). Instrumental broadening was evaluated in the same way from the cerium oxide WAXS reference measurement. The effect of line broadening from the CeO_2 particles itself is negligible because the γ'-precipitates are much smaller than the CeO_2 particles. If it is assumed that the precipitates diffract as coherent domains, the domain size is equal to the particle diameter. The evolution of the particle radius (half domain size) of the γ'-particles with time is shown in Figure 8. For both ageing temperatures, the mean particle radius increases continuously. The selected diffraction peaks could not be fitted well during the first few minutes of ageing. This could be caused by thermal expansion of the sample, and thus a change in investigated volume. Depending on the investigated sample volume, the number of diffracting grains (especially minor phases), changes thus disturbing the peak fitting routine that was used. Once thermal expansion and movement of the sample with respect to the X-ray beam is in equilibrium, the diffraction line broadening analysis is stable.

The results of the SAXS modelling in comparison with the size analysis of γ'-precipitates using WAXS is shown in Figure 8. Good agreement between the mean radius evolutions with ageing time for both ageing temperatures can be seen. This agreement clearly identifies the modelled nano-particles by SAXS to be γ'-precipitates.

In principle, the volume fraction of the γ'-phase can be determined from the WAXS data using various approaches and compared with SAXS results. In the present case, a quantitative volume fraction evaluation was not feasible because of the small number of γ'-particles in the diffracting volume, leading to poor grain averaging (a spotty 2D diffraction pattern). This does not permit a quantitative WAXS intensity analysis, which is needed to determine the volume fraction of the different phases by WAXS.

3.5 Characterization of strengthening

Several strengthening mechanisms are operative at the same time in engineering alloys. The lattice itself hinders the movement of dislocations. The introduction of new dislocations during plastic deformation, foreign particles (precipitates), solutes, and grain size dependency all contribute to strengthening. Normally, it is assumed that the mechanisms can be added linearly and the overall macroscopic yield strength can be written as

$$\sigma_y = \sigma_i + \sigma_{HP} + \sigma_G + \sigma^* + \sigma_{ss} + \sigma_p, \tag{9}$$

where σ_i is the internal friction stress caused by the movement of a dislocation through a perfect lattice (the Peierls–Nabarro stress); σ_{HP} is the Hall-Petch effect (grain size dependency); σ_G results from the disturbances in the lattice caused by immobile dislocations; σ^* is the stress needed to move dislocations past short-range obstacles; σ_{ss} is the solid solution strengthening; and σ_p is the additional stress required to move dislocations around or through precipitates.

Since carbides are present in the initial state of the sample (before ageing), and the diffraction peaks of those carbides do not change significantly during ageing, it can be assumed that variations in precipitate and solid solution strengthening are the dominant contributions to the increase in yield strength during ageing. Therefore, the yield strength at ageing time t, and ageing temperature T can be approximated by

$$\sigma_y(t,T) = \sigma_0(t,T) + \sigma_p(t,T) + \sigma_{ss}(t,T) \tag{10}$$

where σ_0 includes the contribution of strength from other mechanisms. Based on Friedel's statistics for particle spacing, the strengthening contribution of small precipitates can be written as [35]

$$\sigma_p(t,T,f_p) = f_p\sqrt{\phi(t,T)\cdot r_{mean}(t,T)}, \tag{11}$$

where $r_{mean}(t,T)$ is the mean radius, $\phi(t,T)$ is the volume fraction of the precipitates and f_p is a scaling factor. The contribution of solid solution strengthening is correlated with the number of solute atoms in the matrix. A correlation with the difference in volume fraction to the saturation level $\Delta\phi(t,T)$ is found in Section 3.3.3, and is illustrated in Figure 7. From this we can write the solid solution strengthening contribution as

$$\sigma_{ss}(t,T,f_{ss},n,\phi_{max}) = f_{ss}\big(\Delta\phi(t,T)\big)^n = f_{ss}(\phi_{max}(T)-\phi(t,T))^n, \tag{12}$$

where n is an exponential fitting parameter and f_{ss} is a scaling factor. This expression accounts for the solid solution changes during precipitation. By using Eqs (10) – (12) and the measured Vickers hardness data, the unknown parameters in Eqs (11) and (12) can be found by requiring a smooth time dependence of the remaining strengthening contribution σ_o. Thus, the following chi-square has to be minimized

$$\chi^2 = \sum_{i=1}^{2}\sum_{j=2}^{N}\left(\sigma_0(t_{j-1},T_i)-\sigma_0(t_j,T_i)\right)^2, \tag{13}$$

where σ_o is defined by the following expression

$$\sigma_o(t,T,f_p,f_{ss},n,\phi_{max}^T) = 0.33\cdot HV(t,T) - \sigma_p(t,T,f_p) - \sigma_{ss}(t,T,f_{ss},n,\phi_{max}^T). \tag{14}$$

where the yield strength itself is correlated with the Vickers microhardness by $HV\sim 0.33\cdot\sigma_y$ [36]. The outer summation (index i) in Eq. (13) covers the two ageing temperatures (760 and 820°C). The inner summation (index j) covers the accessible times when microhardness and SAXS measurements are available. The global minimum of Eq. (13) is found for the following parameter values: $f_p = 520.7\pm 0.6$ MPa, $f_{ss} = 470.8\ \pm 3.1$ MPa, $n = 0.496\ \pm 0.006$, $\phi_{max}^{760°C} = 0.135\ \pm 0.004$ and $\phi_{max}^{820°C} = 0.141\ \pm 0.001$. Evolution of volume fraction and mean particle radius is determined from the SAXS data as discussed in Section 3.3.3. The evolution of the yield strength and the different strengthening contributions are shown in Figure 9. In region I (dissolution), the precipitate strengthening contribution decreases by roughly 25%, while the solid solution strengthening contribution increases by roughly 50%. The increase in the σ_0 strengthening contribution in region I is caused by crystallization and rearrangement of carbide structures. In region II (nucleation and growth), the solid solution strengthening contribution decreases towards zero while the precipitate strengthening contribution continuously increases. In region III (Ostwald ripening), the solid solution strengthening remains zero while the precipitate strengthening contribution increases further at a slightly smaller rate. Eventually, it should become constant when the alloy reaches its peak hardness. In regions II and III, the σ_0 contribution remains nearly constant indicating that the carbide structures do not significantly change. The separation analysis of the yield strength into the individual contribution confirms that Haynes® 282® is a precipitating hardening alloy.

4 Conclusion

The results provide an understating of how material microstructure develops during heat treatment, and are valuable in developing new accurate material models that can predict yield strength as function of ageing time and temperature. The most important conclusions from this work are:

- A combined high-energy SAXS and WAXS study characterised the isothermal precipitate kinetics of γ'-phase in Haynes® 282® superalloy at 760 and 820°C. A time resolution of 2 s for SAXS, and 0.3 s for WAXS was achieved. The time resolution achieved permits the various precipitation stages (dissolution, nucleation, growth and coarsening) of the γ'-particles to be measured with high precision.
- The WAXS data reveal that there are several phases present in the alloy at room temperature: the matrix itself γ, the precipitate phase γ', the metallic carbide MC, and secondary metallic carbides $M_{23}C_6$ and/or M_6C. The WAXS data indicated that small angle scattering is mainly produced by the γ'-precipitate phase.
- The evolution of volume fraction, number density, and size distribution of the γ'-precipitates were determined from the high-energy SAXS measurements without knowing the composition of the precipitates. The parameters were computed from a set of equations (Eq. (5)), derived from the computed invariant Q_{inv} and third moment of the size distribution $\langle R^3 \rangle$. This solution procedure is believed to decrease the scatter in the results caused by experimental uncertainties, since the fitted model averages small fluctuations in the measured data.
- *Ex-situ* Vickers microhardness measurements showed that the peak hardness strongly depends on the ageing temperature.
- The *ex-situ* Vickers microhardness measurements can be explained by a superposition of precipitate, solid solution strengthening and carbide strengthening components. The time dependence of the components is quantitatively determined by nano- and microstructural parameters evaluated from the SAXS data.

The combined high X-ray energy SAXS and WAXS study performed and the associated evaluation process indicate the potential to predict macroscopic properties of superalloys, such as Vickers microhardness, based on micro- and nanostructure parameters. Knowledge of linking nanostructure parameters with macroscopic properties will enable further development of finite element simulation frameworks to reliably predict superalloy behaviour under different external conditions such as temperature and load.

5 Acknowledgements

The authors would like to thank Mr Anton Denzler, Hans Gruber, Jonas Henrikson and Manne Solbreck for performing the Vickers microhardness testing. Financial support from the strategic innovation programme LIGHTer provided by VINNOVA, funding via the Swedish National Aviation Engineering Research Programme provided by VINNOVA, as well as the SSF-project Additive Manufacturing - Development of Process and Materials (GMT14-0048), are acknowledged. The use of the Advanced Photon Source was supported by the U.S. DOE under Contract No.: DEAC02-06CH11357. The authors would like to thank Jon Almer for his support of the SAXS/WAXS experiments as well as John Christopher Ion for language revision of the manuscript.

References

[1] C.T. Sims, N.S. Stoloff, W.C. Hagel, Superalloys II, John Wiley & Sons, 1987.

[2] H. White, M. Santella, E.D. Specht, Weldability of HAYNES 282 alloy for new fabrications and

after service exposure, Energy Mater. Mater. Sci. Eng. Energy Syst. 4 (2009) 84–91. doi:10.1179/174892310X12811032100114.

[3] L.M. Pike, Development of a fabricable gamma-prime (γ′) strengthened superalloy, Proc. Int. Symp. Superalloys. (2008) 191–200. doi:10.7449/2008/Superalloys_2008_191_200.

[4] G.R. Holcomb, P.D. Jablonski, P. Wang, Cast Alloys for Advanced Ultra Supercritical Steam Turbines, in: Superalloy 718 Deriv., John Wiley & Sons, Inc., Hoboken, NJ, USA, 2012: pp. 946–960. doi:10.1002/9781118495223.ch72.

[5] L.M. Pike, Long Term Thermal Exposure of HAYNES 282 Alloy, in: Superalloy 718 Deriv., John Wiley & Sons, Inc., Hoboken, NJ, USA, 2012: pp. 644–660. doi:10.1002/9781118495223.ch50.

[6] J. Andersson, G. Sjöberg, M. Chaturvedi, Hot Ductility Study of HAYNES(®) 282(®) Superalloy, in: E.A. Ott, J.R. Groh, A. Banik, I. Dempster, T.P. Gabb, R. Helmink, et al. (Eds.), Superalloy 718 Deriv., John Wiley & Sons, Inc., Hoboken, NJ, USA, 2012: pp. 538–554. doi:10.1002/9781118495223.ch41.

[7] A. Ghoneim, O.A. Ojo, Transient Liquid Phase Bonding of Newly Developed HAYNES 282 Superalloy, in: Superalloy 718 Deriv., John Wiley & Sons, Inc., Hoboken, NJ, USA, 2012: pp. 427–438. doi:10.1002/9781118495223.ch33.

[8] S.C. Longanbach, C.J. Boehlert, The Creep and Fatigue Behavior of Haynes 282 at Elevated Temperatures, in: Superalloy 718 Deriv., John Wiley & Sons, Inc., Hoboken, NJ, USA, 2012: pp. 555–557. doi:10.1002/9781118495223.ch42.

[9] P.D. Jablonski, C.J. Cowen, J.A. Hawk, Effects of Al and Ti on Haynes 282 with Fixed Gamma Prime Content, in: Superalloy 718 Deriv., John Wiley & Sons, Inc., Hoboken, NJ, USA, 2012: pp. 616–628. doi:10.1002/9781118495223.ch48.

[10] L.O. Osoba, R.G. Ding, O.A. Ojo, Microstructural analysis of laser weld fusion zone in Haynes 282 superalloy, Mater. Charact. 65 (2012) 93–99. doi:10.1016/j.matchar.2011.12.009.

[11] M. Fisk, J. Andersson, R. du Rietz, S. Haas, S. Hall, Precipitate evolution in the early stages of ageing in Inconel 718 investigated using small-angle x-ray scattering, Mater. Sci. Eng. A. 612 (2014) 202–207. doi:10.1016/j.msea.2014.06.036.

[12] J.E. Daniels, D. Pontoni, R.P. Hoo, V. Honkimäki, Simultaneous small-and wide-angle scattering at high X-ray energies, J. Synchrotron Radiat. 17 (2010) 473–478. doi:10.1107/S0909049510016456.

[13] S.D. Shastri, Combining flat crystals, bent crystals and compound refractive lenses for high-energy X-ray optics, J. Synchrotron Radiat. 11 (2004) 150–156. doi:10.1107/S0909049503023586.

[14] J.H. Lee, C.C. Aydıner, J. Almer, J. Bernier, K.W. Chapman, P.J. Chupas, et al., Synchrotron applications of an amorphous silicon flat-panel detector, J. Synchrotron Radiat. 15 (2008) 477–488. doi:10.1107/S090904950801755X.

[15] P. Delogu, P. Oliva, R. Bellazzini, A. Brez, P.L. de Ruvo, M. Minuti, et al., Characterization of Pixirad-1 photon counting detector for X-ray imaging, J. Instrum. 11 (2016) P01015–P01015. doi:10.1088/1748-0221/11/01/P01015.

[16] H. Matysiak, M. Zagorska, J. Andersson, A. Balkowiec, R. Cygan, M. Rasinski, et al., Microstructure of Haynes® 282® Superalloy after Vacuum Induction Melting and Investment Casting of Thin-Walled Components, Materials (Basel). 6 (2013) 5016–5037.

doi:10.3390/ma6115016.

[17] H.M. Rietveld, A profile refinement method for nuclear and magnetic structures, J. Appl. Crystallogr. 2 (1969) 65–71. doi:10.1107/S0021889869006558.

[18] L. Lutterotti, S. Matthies, H.-R. Wenk, MAUD, (1999). http://maud.radiographema.eu/.

[19] G. Ashiotis, A. Deschildre, Z. Nawaz, J.P. Wright, D. Karkoulis, F.E. Picca, et al., The fast azimuthal integration Python library: pyFAI, J. Appl. Crystallogr. 48 (2015) 510–519. doi:10.1107/S1600576715004306.

[20] F. Zhang, J. Ilavsky, G.G. Long, J.P.G. Quintana, A.J. Allen, P.R. Jemian, Glassy Carbon as an Absolute Intensity Calibration Standard for Small-Angle Scattering, Metall. Mater. Trans. A. 41 (2010) 1151–1158. doi:10.1007/s11661-009-9950-x.

[21] W. Woo, V. Em, E. Shin, P. Mikula, V. Ryukhtin, Influence of multiple small-angle neutron scattering on diffraction peak broadening in ferritic steel, J. Appl. Crystallogr. 48 (2015) 350–356. doi:10.1107/S1600576715000813.

[22] Y. Yang, R.C. Thomson, Microstructural evolution in cast Haynes 282 for applications in advanced power plants, in: D. Gandy, J. Shingledecker (Eds.), Adv. Mater. Technol. Foss. Power Plants, ASM International, 2014: pp. 143–154.

[23] H. White, M. Santella, E.D. Specht, Weldability of HAYNES 282 alloy for new fabrications and after service exposure, Energy Mater. 4 (2009) 84–91. doi:10.1179/174892310X12811032100114.

[24] J.A. Hawk, T.-L. Cheng, J.S. Sears, P.D. Jablonski, Y.-H. Wen, Gamma Prime Stability in Haynes 282: Theoretical and Experimental Considerations, J. Mater. Eng. Perform. 24 (2015) 4171–4181. doi:10.1007/s11665-015-1711-y.

[25] D.H. Bechetti, J.N. DuPont, J.A. Siefert, J.P. Shingledecker, Microstructural Evolution and Creep-Rupture Behavior of A-USC Alloy Fusion Welds, Metall. Mater. Trans. A. 47 (2016) 4502–4518. doi:10.1007/s11661-016-3603-7.

[26] C. Joseph, Microstructural characterization of Haynes 282 after heat treatment and forging, Chalmers University of Technology, 2015.

[27] A. Vrij, Mixtures of hard spheres in the Percus–Yevick approximation. Light scattering at finite angles, J. Chem. Phys. 71 (1979) 3267. doi:10.1063/1.438756.

[28] J.S. Pedersen, Analysis of small-angle scattering data from colloids and polymer solutions: modeling and least-squares fitting, Adv. Colloid Interface Sci. 70 (1997) 171–210. doi:10.1016/S0001-8686(97)00312-6.

[29] L.B. Kiss, J. Söderlund, G.A. Niklasson, C.G. Granqvist, The real origin of lognormal size distributions of nanoparticles in vapor growth processes, Nanostructured Mater. 12 (1999) 327–332. doi:10.1016/S0965-9773(99)00128-2.

[30] R.B. Bergmann, A. Bill, On the origin of logarithmic-normal distributions: An analytical derivation, and its application to nucleation and growth processes, J. Cryst. Growth. 310 (2008) 3135–3138. doi:10.1016/j.jcrysgro.2008.03.034.

[31] J.S. Pedersen, Determination of size distribution from small-angle scattering data for systems with effective hard-sphere interactions, J. Appl. Crystallogr. 27 (1994) 595–608. doi:10.1107/S0021889893013810.

[32] J.K. Percus, G.J. Yevick, Analysis of Classical Statistical Mechanics by Means of Collective Coordinates, Phys. Rev. 110 (1958) 1–13. doi:10.1103/PhysRev.110.1.

[33] O. Glatter, O. Kratky, Small Angle X-ray Scattering, Academic Press, 1982.

[34] D. Balzar, Defect and Microstructure Analysis from Diffraction, Oxford University Press, 1999.

[35] A. Deschamps, F. Livet, Y. Bréchet, Influence of predeformation and ageing of an Al–Zn–Mg alloy—II. Modeling of precipitation kinetics and yield stress, Acta Mater. 47 (1998) 293–305. doi:10.1016/S1359-6454(98)00296-1.

[36] O.R. Myhr, Ø. Grong, Modelling of the microstructure and strength evolution in Al – Mg – Si alloys during multistage thermal processing, Acta Mater. 52 (2004) 4997–5008. doi:10.1016/j.actamat.2004.07.002.

Tables:

Table 1: Measured lattice parameter of the identified phases in the initial Haynes® 282® sample.

Phase	**ICSD[1] code**	**a_0 (nm) measured**	**a_0 (nm) ICSD file**
γ / Fm-3m (225)	103559	0.3587	0.3575
γ' / Pm-3m (221)	608782	0.3585	0.3580
$M_{23}C_6$ / Fm-3m (225)	156148	1.0736	1.1023
MC / Fm-3m (225)	77168	0.4304	0.4308

---

[1] Inorganic Crystal Structure Database.

Figures:

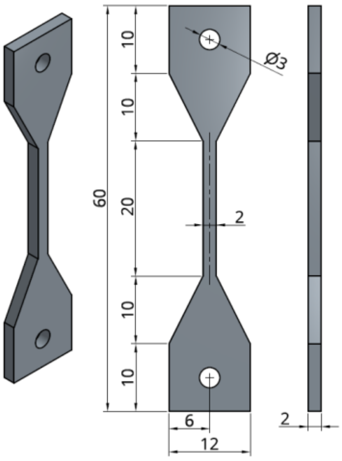

Figure 1: Sample geometry of specimen used in SAXS/WAXS experiment.

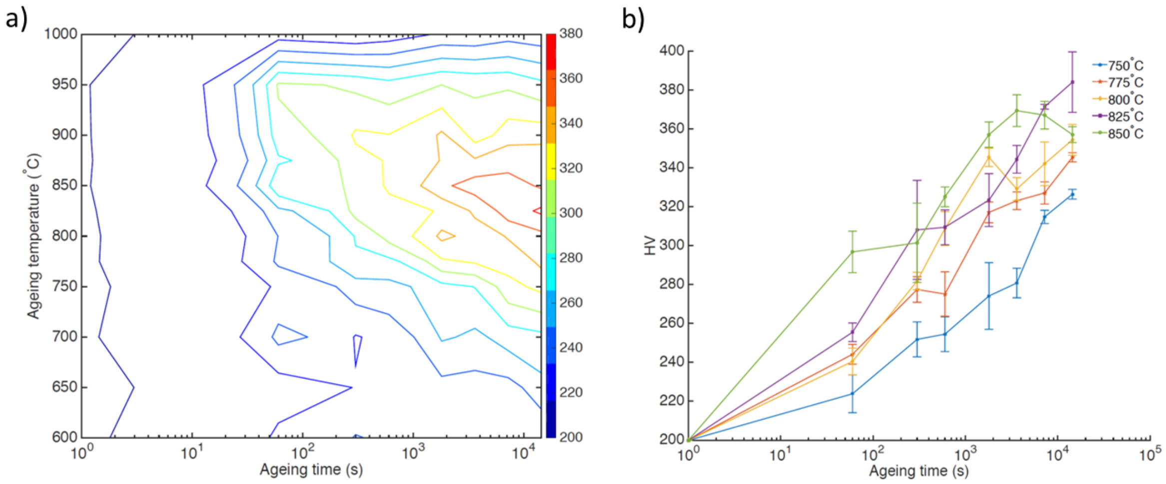

Figure 2: Vickers microhardness measurements. (a) Contour plot of ageing time, temperature and microhardness. (b) Variation in hardness with ageing time at five elevated temperatures.

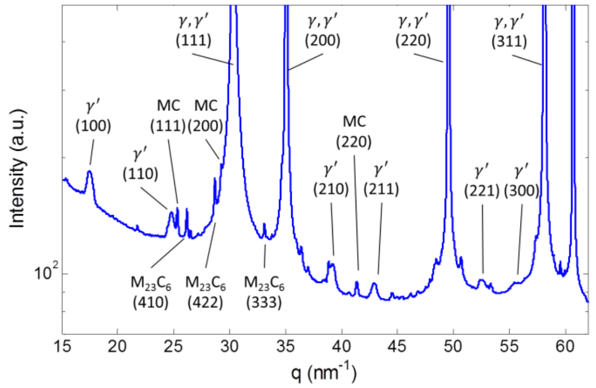

Figure 3: High energy X-ray diffraction pattern obtained at room temperature from the initial sample. Intensity is shown on a logarithmic scale to emphasize weak reflections.

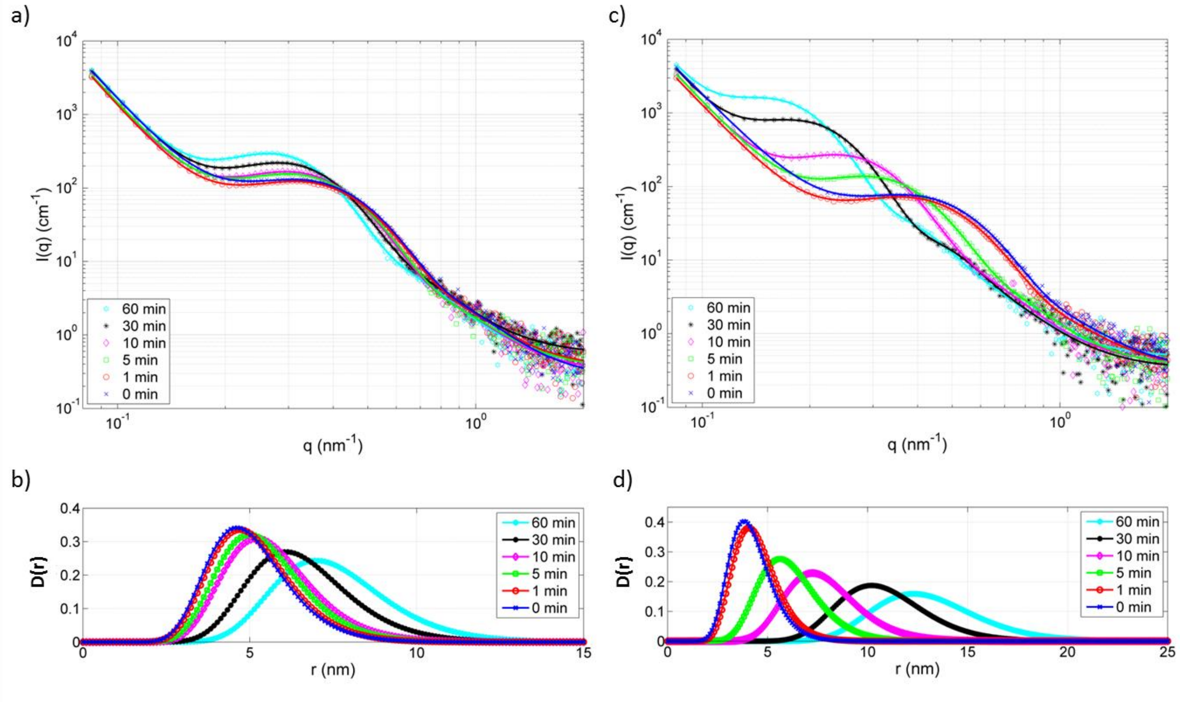

Figure 4: Differential scattering cross sections for samples aged at 760°C (a) and 820°C (c). The symbols represent experimental data and the solid lines are the model curves. The corresponding lognormal size distributions are shown in (b) and (d).

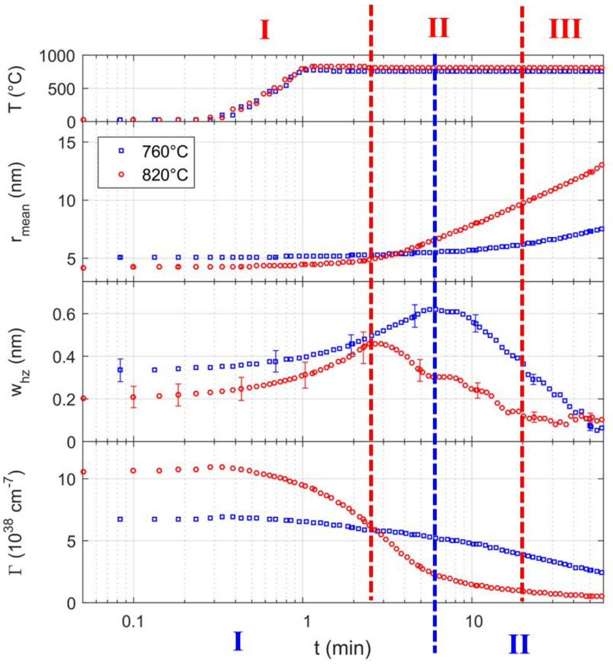

Figure 5: The evolution (from top to bottom) of temperature $\boldsymbol{T}$, mean radius $\boldsymbol{r_{mean}}$, repulsion zone width $\boldsymbol{w_{hz}}$, and scale factor $\boldsymbol{\Gamma}$ for samples isothermally aged at 760 and 820°C, respectively. The number of plotted data points is reduced for conciseness.

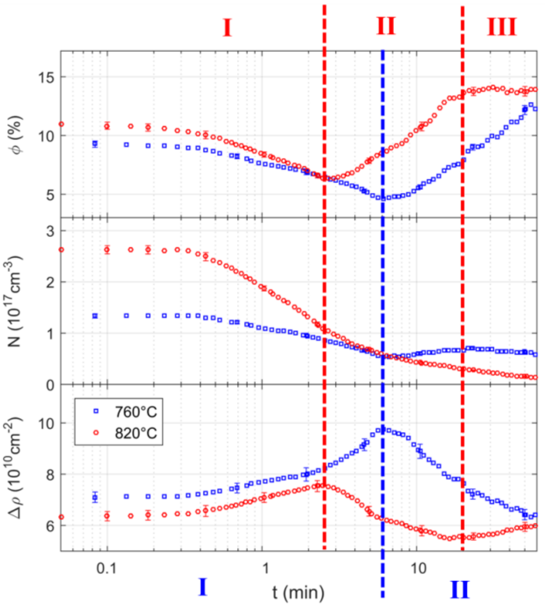

Figure 6: The time evolution (from top to bottom) of temperature $\boldsymbol{T}$, volume fraction $\boldsymbol{\phi}$, number density $\boldsymbol{N}$ and scattering contrast $\boldsymbol{\Delta\rho}$ of the precipitates.

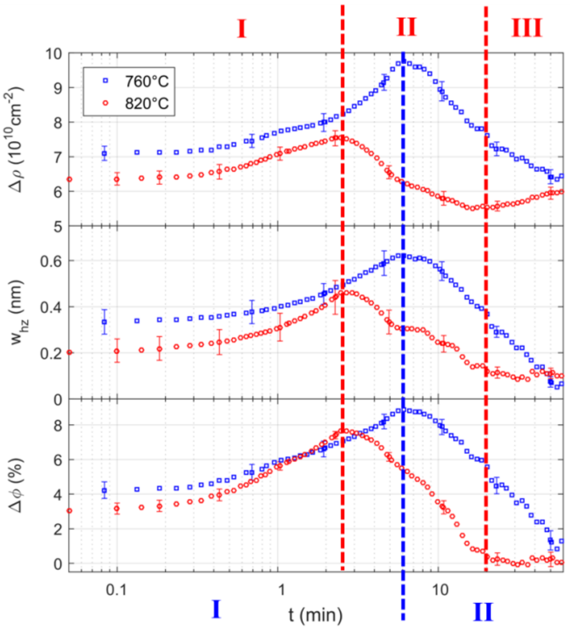

Figure 7: The time evolution of the scattering contrast $\boldsymbol{\Delta\rho}$, repulsion zone width $\boldsymbol{w_{hz}}$ and difference of volume fraction to the saturation level $\boldsymbol{\Delta\phi}$ of the precipitates.

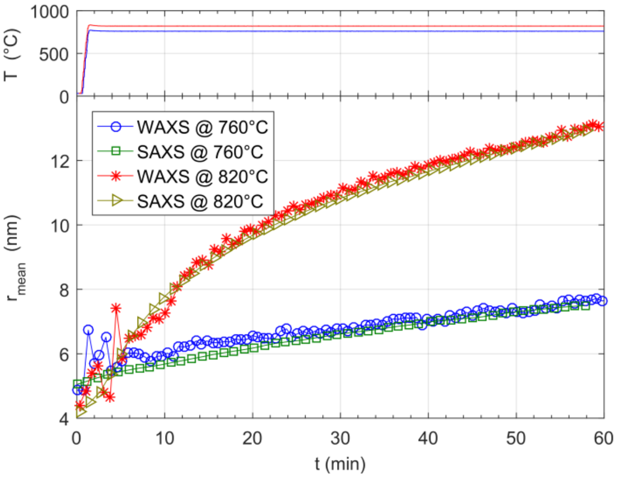

Figure 8: Comparison of precipitate size determined by WAXS (open circle and star symbol) and SAXS (open square and open hexagon symbol) for the two ageing temperatures 760 and 820°C, respectively.

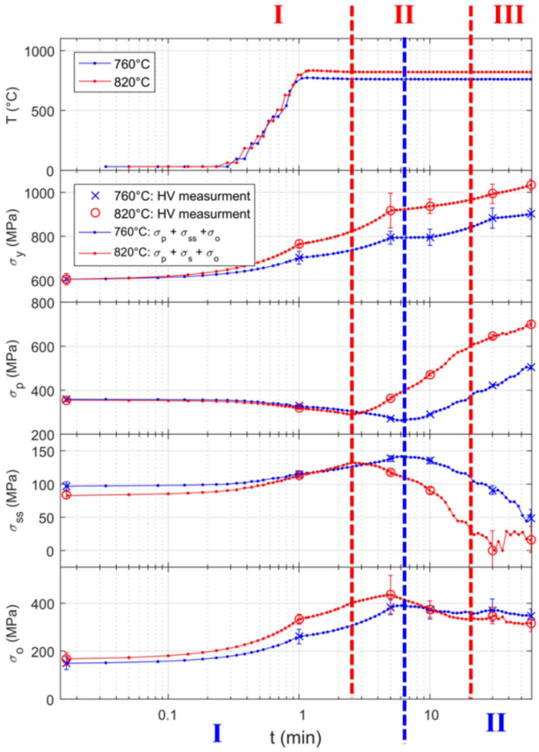

Figure 9**:** The evolution (from top to bottom) of temperature $\boldsymbol{T}$, yield strength $\boldsymbol{\sigma_y}$, precipitate strengthening $\boldsymbol{\sigma_p}$, solid solution strengthening $\boldsymbol{\sigma_{ss}}$ and initial (carbide) strengthening contribution $\boldsymbol{\sigma_o}$ for samples aged at 760 and 820°C, respectively. The open symbols are *ex situ* hardness measurements, and the lines are computed from the SAXS results. Except for the carbide strengthening contribution where the accessible data points are linear interpolated.

Supplementary Information

Correlation of precipitation kinetics and Vickers hardness in Haynes® 282® superalloy: *In situ* high-energy SAXS/WAXS study

Sylvio Haas[1,a], Joel Andersson[2,b], Martin Fisk[3,c,d], Jun-Sang Park[4,e], Ulrich Lienert[5,a]

[a]Photon Science, DESY, Hamburg, Germany

[b]Department of Engineering Science, University West, Trollhättan, Sweden

[c]Materials Science and Applied Mathematics, Malmö University, Malmö, Sweden

[d]Division of Solid Mechanics, Lund University, P.O. Box 118, SE-221 00 Lund, Sweden

[e]X-ray Science Division, Advanced Photon Source, Argonne National Laboratory, USA

[1]Sylvio.Haas@desy.de, [2]Joel.Andersson@hv.se, [3]Martin.fisk@mah.se, [4]parkjs@aps.anl.gov, [5]Ulrich.Lienert@desy.de

1 Composition of the Haynes® 282® samples

Table 1: Nominal composition in wt%.

Alloy	Al	B	C	Nb	Co	Cr	Cu	Fe	Mn	Mo	Ni	P	S	Si	Ti	Ta	W
Haynes® 282®	1.52	0.005	0.072	-	10.36	19.49	<0.01	0.37	0.05	8.55	Bal.	<0.002	<0.002	<0.05	2.16	<0.01	<0.01
Alloy 718	0.58	0.004	0.067	4.93	0.55	18.10	0.07	18.50	0.23	3.06	53.10	<0.005	<0.002	0.06	1.03	<0.05	

2 X-ray transmission of samples aged at 760 and 820°C

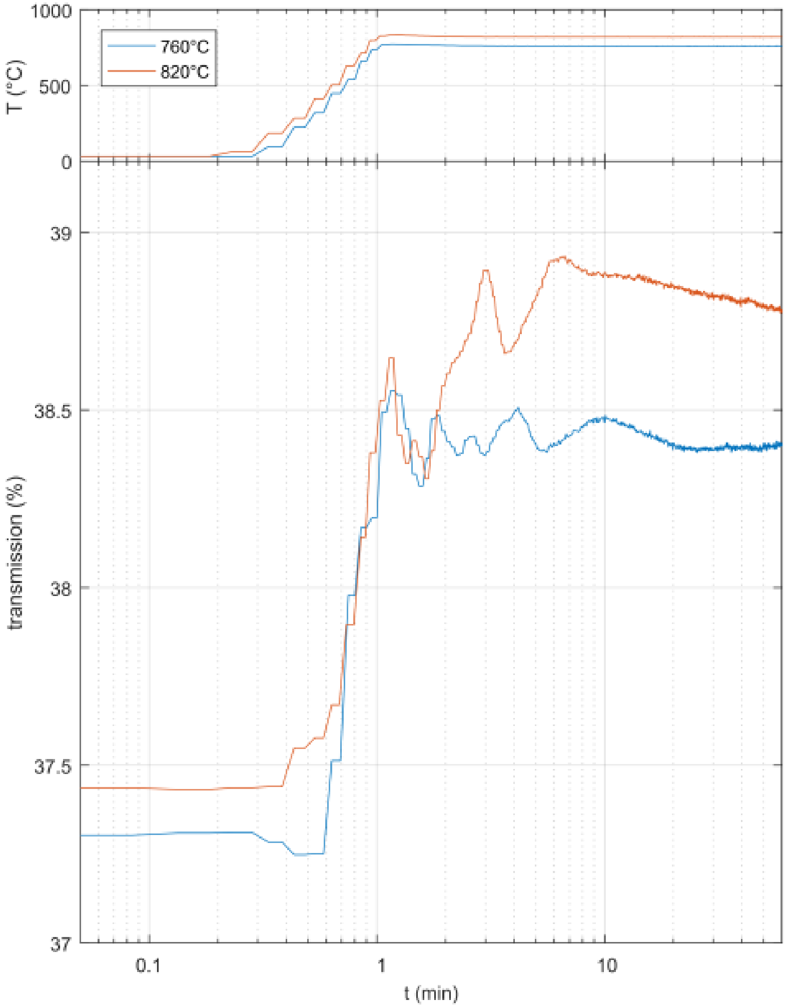

Figure S1: X-ray transmission as function of ageing time for the samples aged at 760 and 820°C, respectively.

3 Experimental versus model SAXS intensities

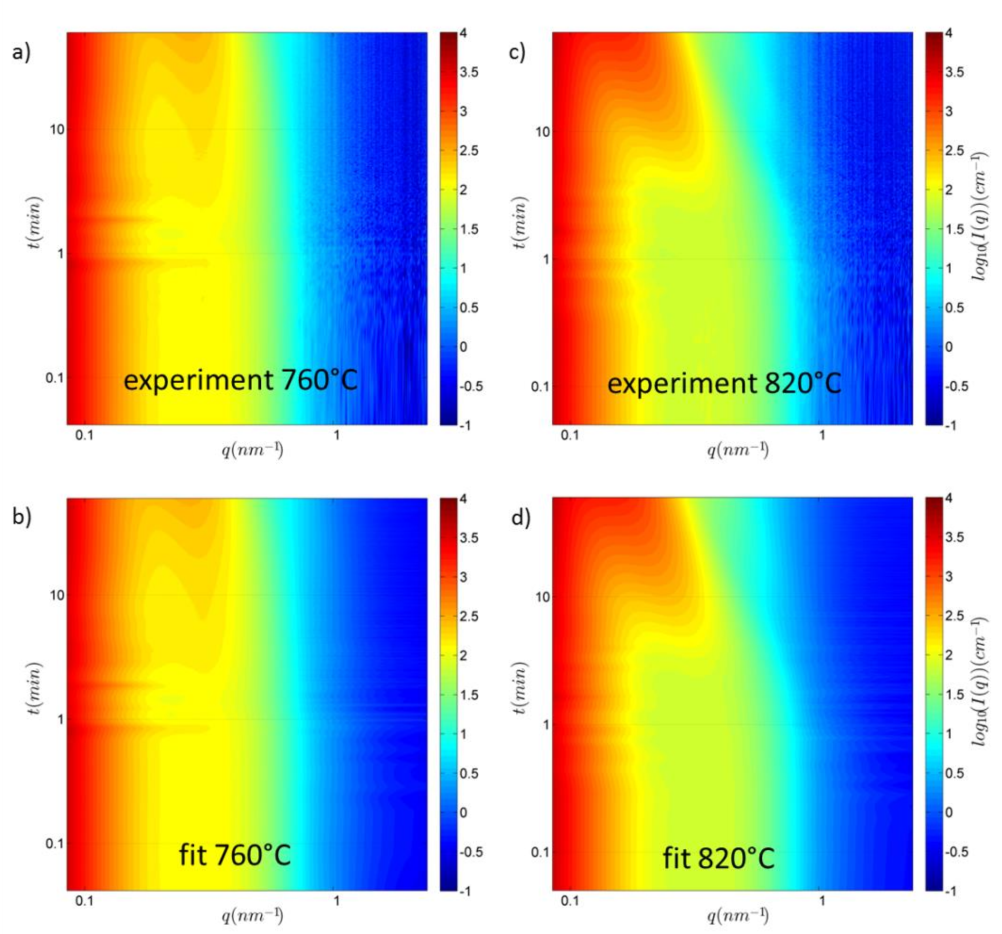

Figure S2: Comparison of the measured and modelled SAXS pattern of the Haynes 282 samples aged at 760 and 820°C

4 Time evolution of precipitate size distribution

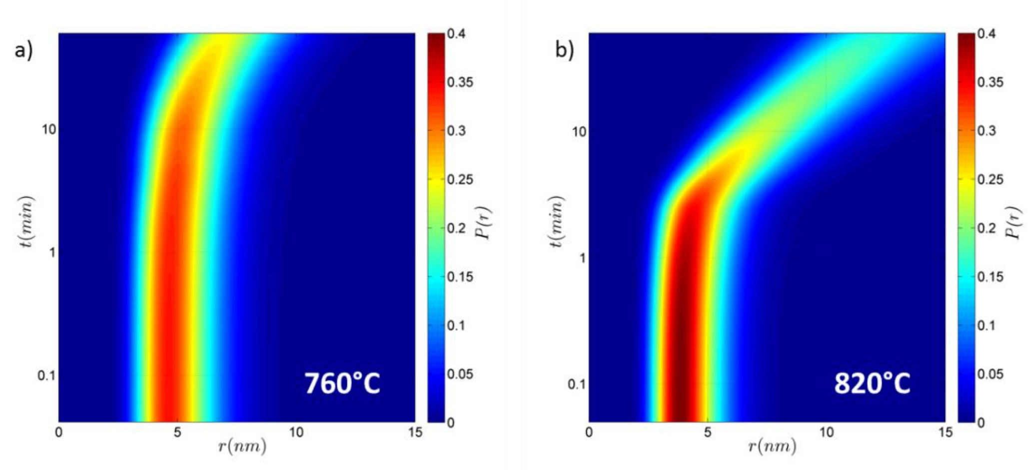

Figure S3: Comparison of the evolution of the lognormal size distribution of precipitates obtained by SAXS modelling. In both cases an increase in size can be seen.

5 Time evolution of the nanostructure parameters determined by the SAXS analysis

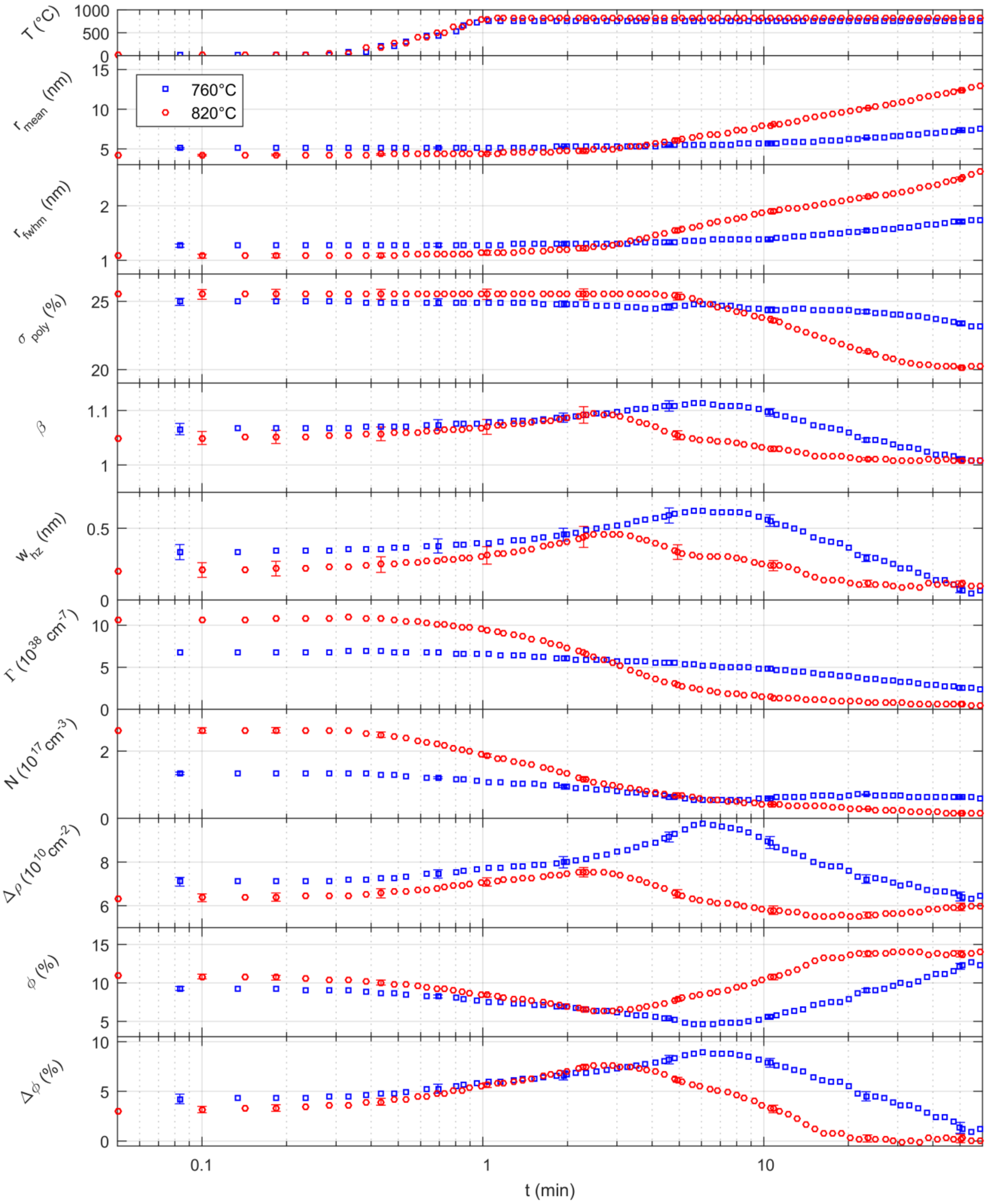

Figure S4: Time evolution of the SAXS model parameters for the samples aged at 760 and 820°C, respectively. The number of plotted data points is reduced and for every 10th point the error bar is also shown.

6 Time evolution of the change in number density of precipitates

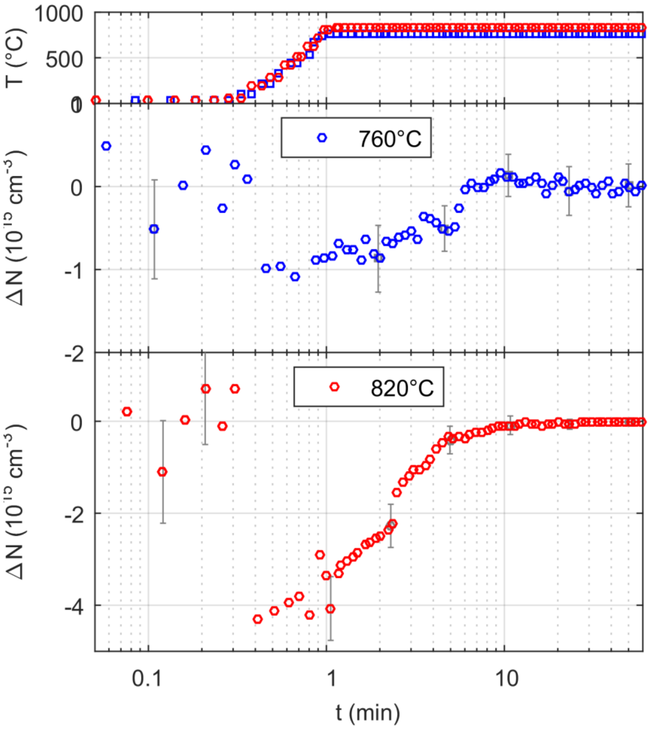

Figure S5: Time evolution of the change in number density as a function of ageing time. Depending on the ageing regime different slopes can be identified.

7 WAXS diffraction pattern at room temperature

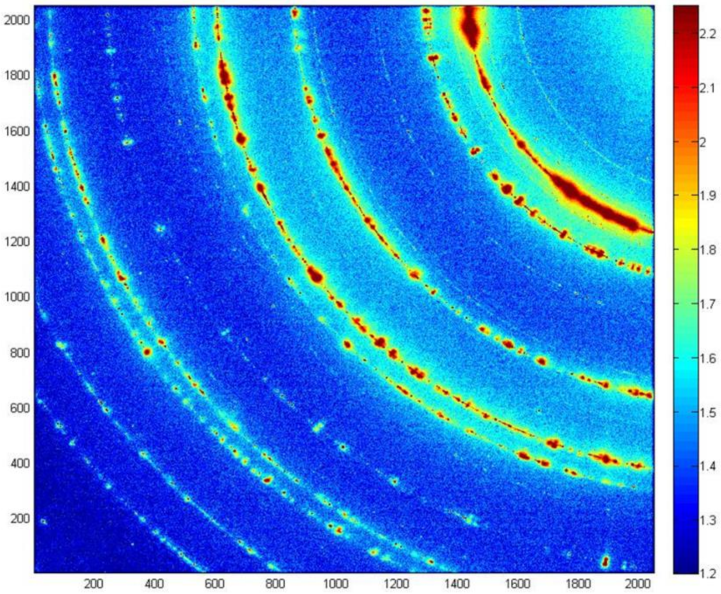

Figure S6: WAXS detector image of one sample at room temperature. The diffraction pattern contains many spots, indicating that the number of diffracting grains is insufficient for quantitative intensity evaluation.

8 Time evolution of the orientation-integrated WAXS patterns

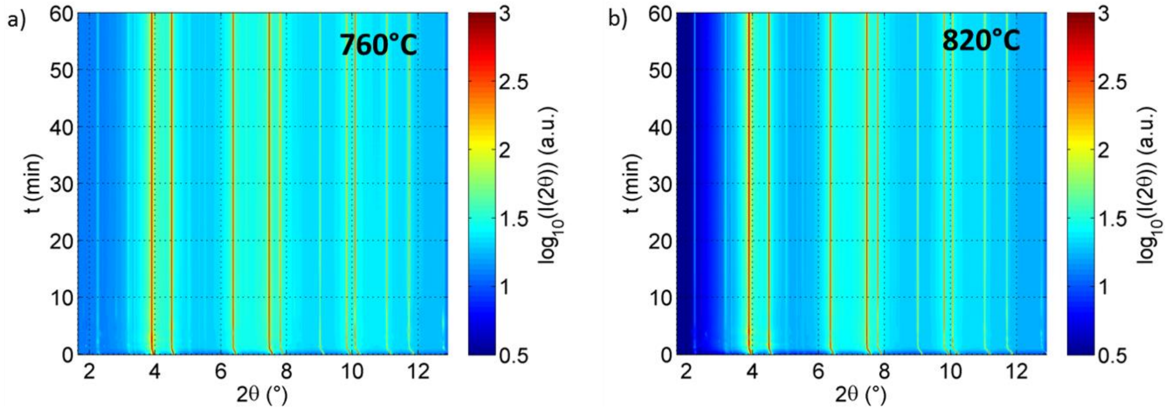

Figure S7: Evolution of WAXS pattern as function of ageing time. During heating the sample from room temperature to the ageing temperature the peaks are shifted towards smaller angles, which is caused by thermal expansion. During isothermal heating the position of the diffraction peaks does not change significantly. Only the peak width of the γ'-phase Bragg reflections decreases resulting from the growth of particles.

9 Explanation of repulsion zone around precipitates

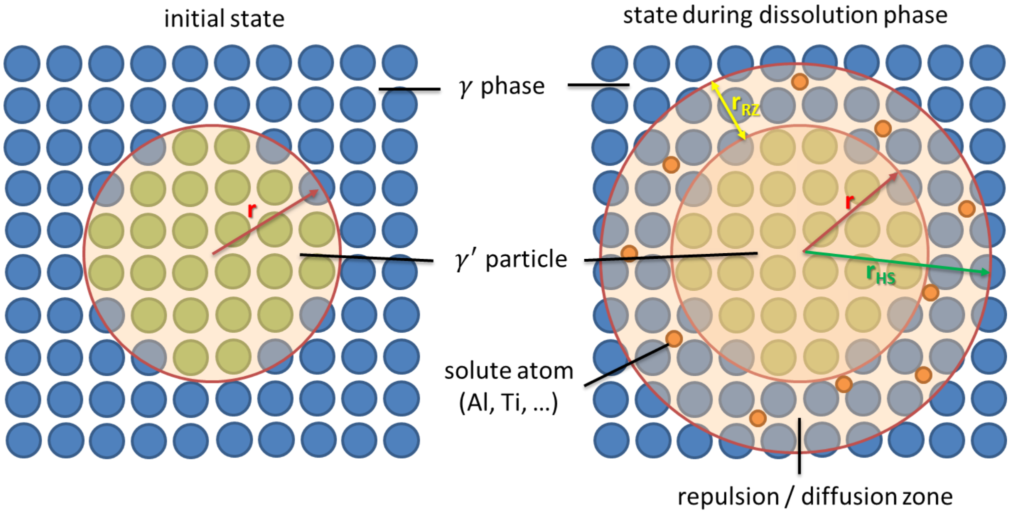

Figure S8: Schematic of the repulsion zone around a dissolving precipitate. In the repulsion zone the concentration of solute atoms is higher and therefore higher local strain fields exist, which hinder the movement of dislocations.